

Supplementary Figures

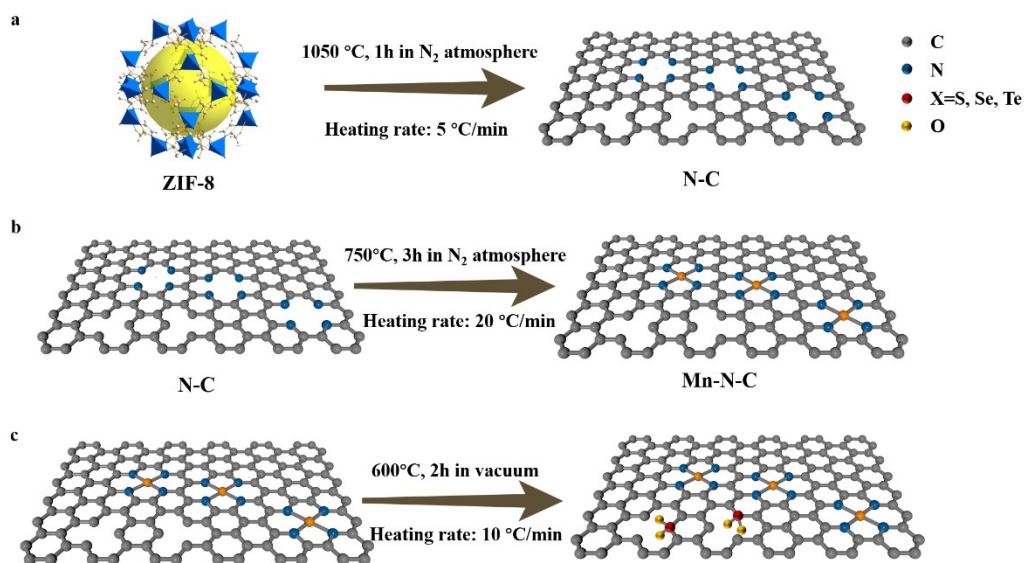


Figure S1. Schematic diagram of the synthesis of N-C, Mn-N-C, and Mn-N-C/XO₂ catalysts.

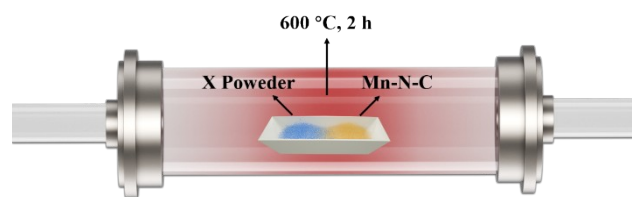


Figure S2. Schematic diagram of experimental apparatus for fabricating Mn-N-C/XO₂ (X=S, Se and Te) catalysts. Note that 1 g of X powder were placed upstream in the tube, while 30 mg of Mn-N-C catalyst powder was placed 1 cm downstream of the tube center. During synthesis, the tube furnace was held at 600 °C for 2 h, and both ends of the tube were sealed.

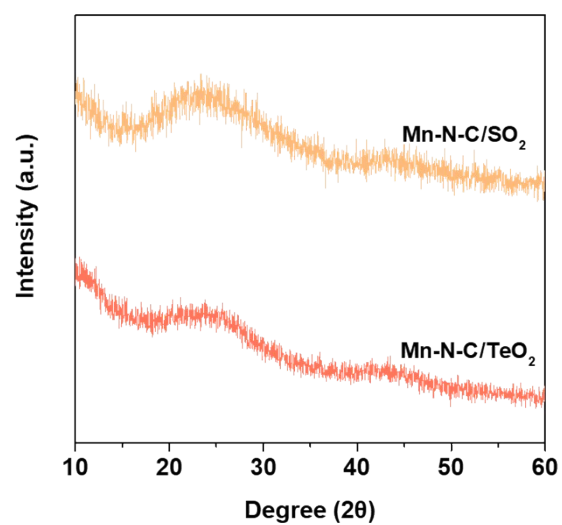


Figure S3. XRD spectrum of Mn-N-C/SO₂ and Mn-N-C/TeO₂ catalyst. As shown, after the incorporation of XO₂, the XRD patterns still only show the carbon (0 0 2) and (1 1 0) peaks, indicating that Mn remains atomically dispersed within the carbon matrix even after XO₂ incorporation.

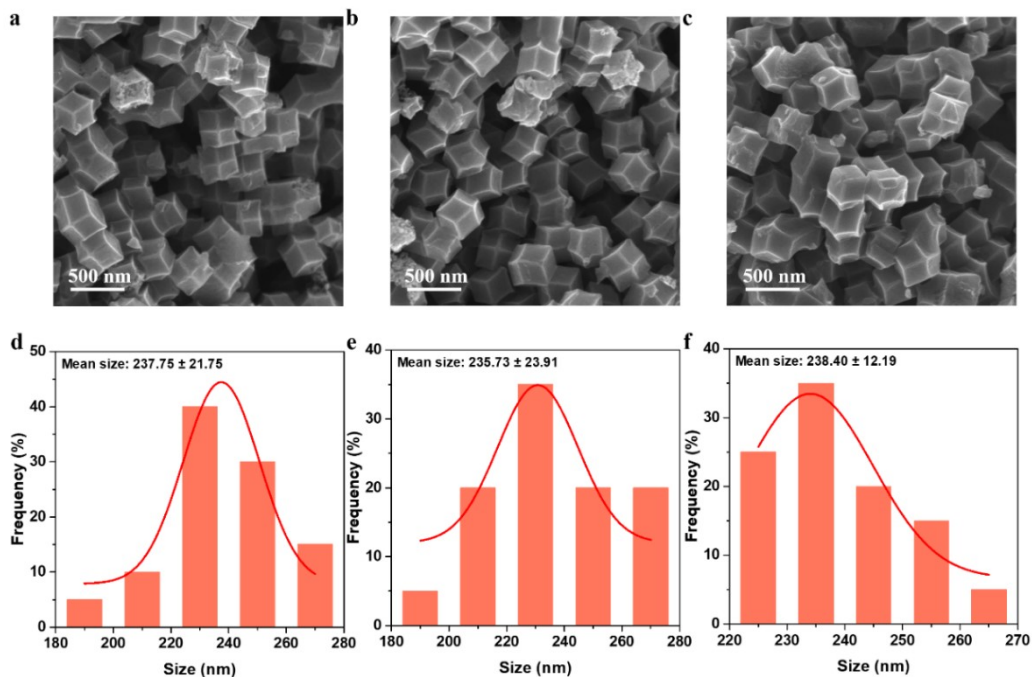


Figure S4. SEM image of (a) Mn-N-C, (b) Mn-N-C/SO₂ and (c) Mn-N-C/TeO₂ catalysts, size distribution of (d) Mn-N-C, (e) Mn-N-C/SO₂ and (f) Mn-N-C/TeO₂ catalysts. As illustrated, the Mn-N-C catalyst particles exhibit an average diameter of 237.75 nm. After the incorporation of XO₂, the average diameter of the Mn-N-C/XO₂ catalyst particles shows no significant change compared to that of the Mn-N-C catalyst (Mn-N-C/SO₂: 235.73 nm, Mn-N-C/SeO₂: 238.09 nm as shown in Figure R2 and inset, Mn-N-C/TeO₂: 238.40 nm).

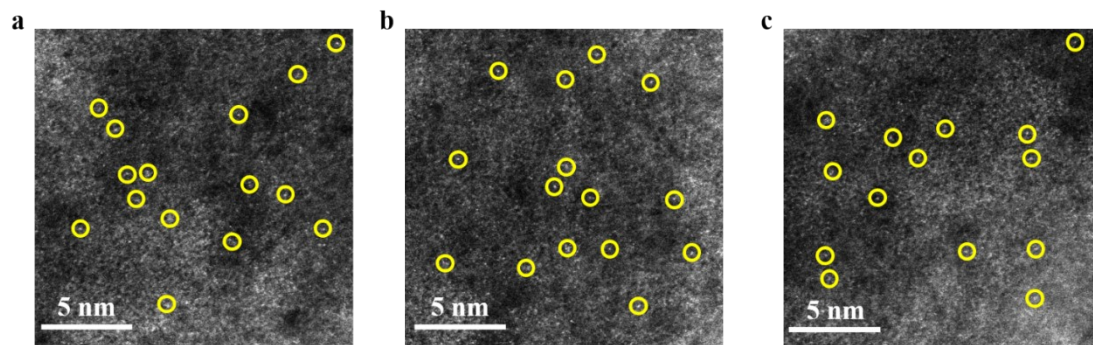


Figure S5. HADDF-STEM images of (a) Mn-N-C, (b) Mn-N-C/SO₂, and (c) Mn-N-C/TeO₂. The Mn single atoms were marked with yellow circles.

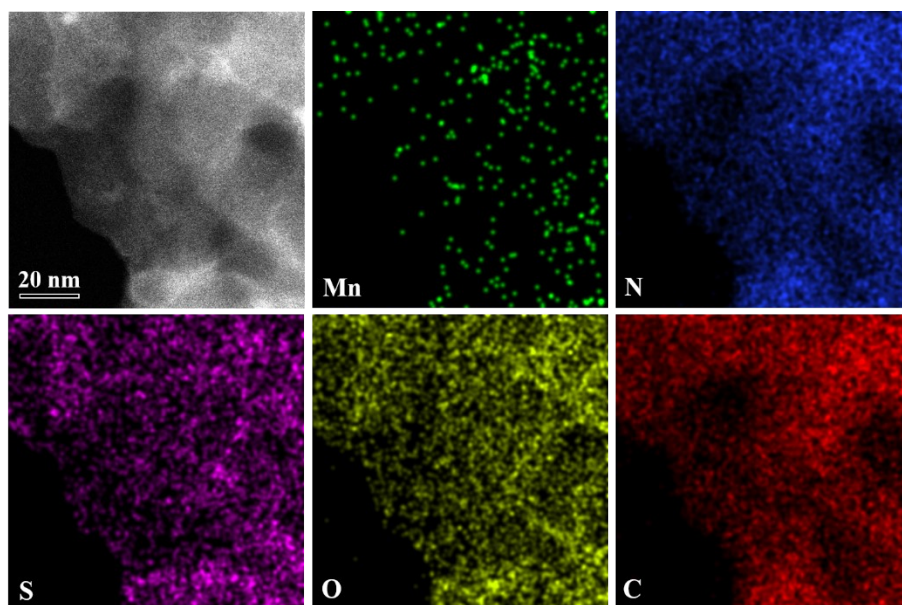


Figure S6. HADF-STEM images of Mn-N-C/SO₂ and the corresponding EDS mappings of Mn, N, S, O and C elements.

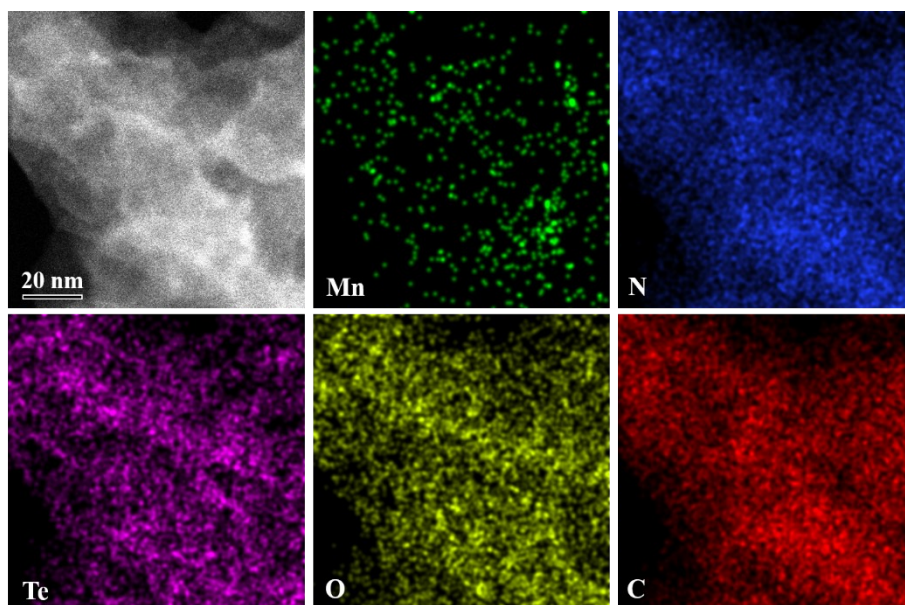


Figure S7. HADF-STEM images of Mn-N-C/TeO₂ and the corresponding EDS mappings of Mn, N, Te, O and C elements.

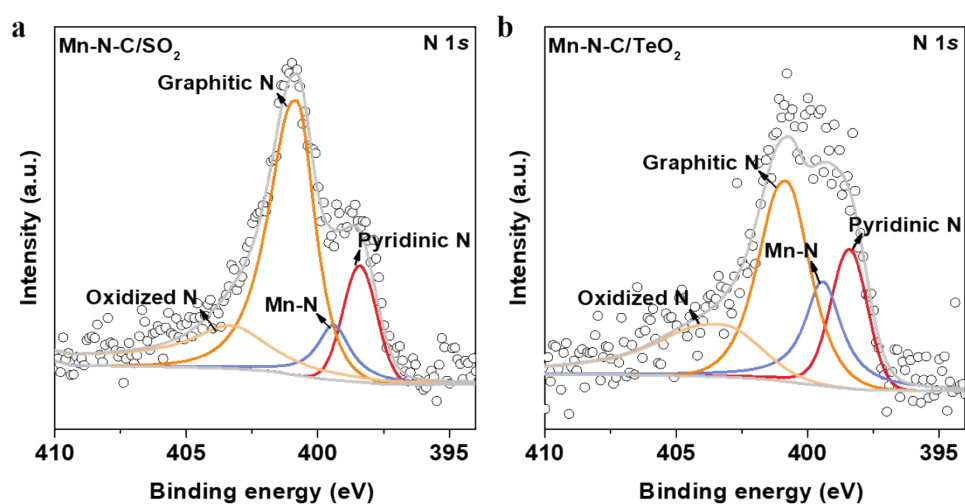


Figure S8. N 1s XPS spectra of (a) Mn-N-C/SO₂ and (b) Mn-N-C/TeO₂ catalysts. The peak positions show no significant changes, confirming that the incorporation of XO₂ does not alter the Mn-N₄ coordination structure of the metal atom Mn.

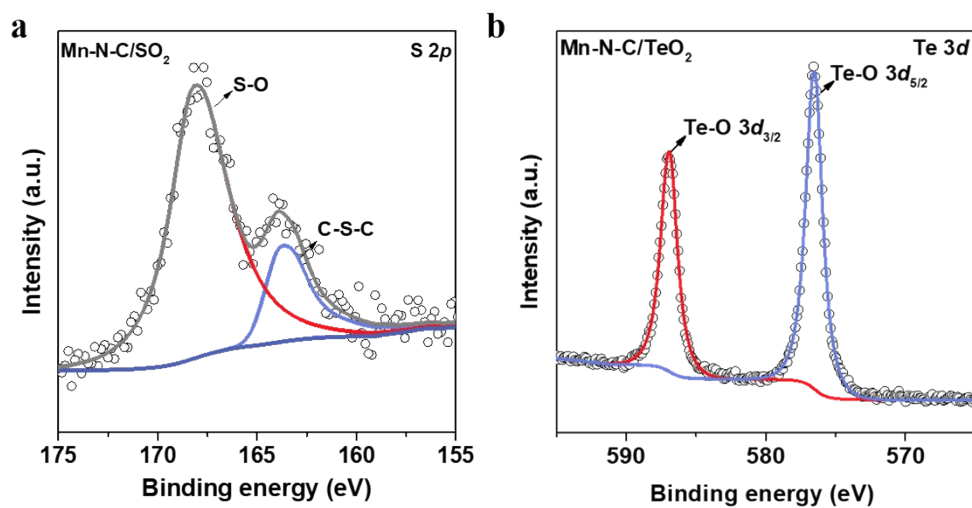


Figure S9. (a) S 2p XPS spectrum of Mn-N-C/SO₂. (b) Te 3d XPS spectrum of Mn-N-C/TeO₂. As shown in this figure and Figure 2c, almost all the X added to the carbon matrix is oxidized to XO₂.

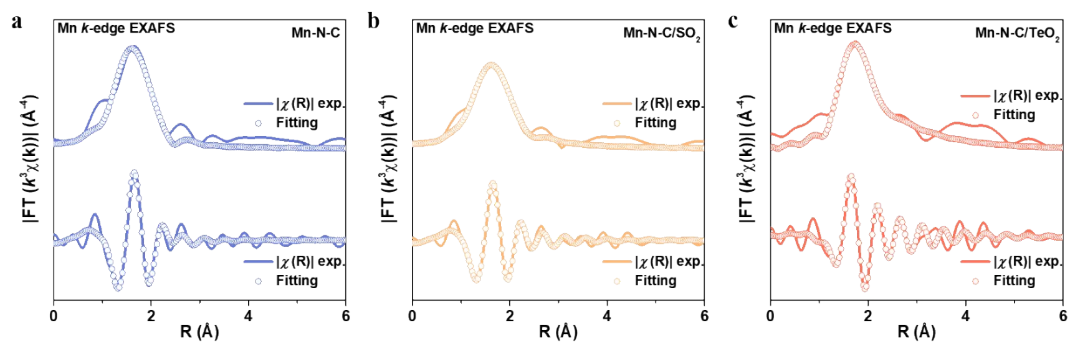


Figure S10. FT-EXAFS of the experimental and fitted Mn K-edge spectra of (a) Mn-N-C, (b) Mn-N-C/SO₂ and (c) Mn-N-C/TeO₂ catalysts in R space, respectively.

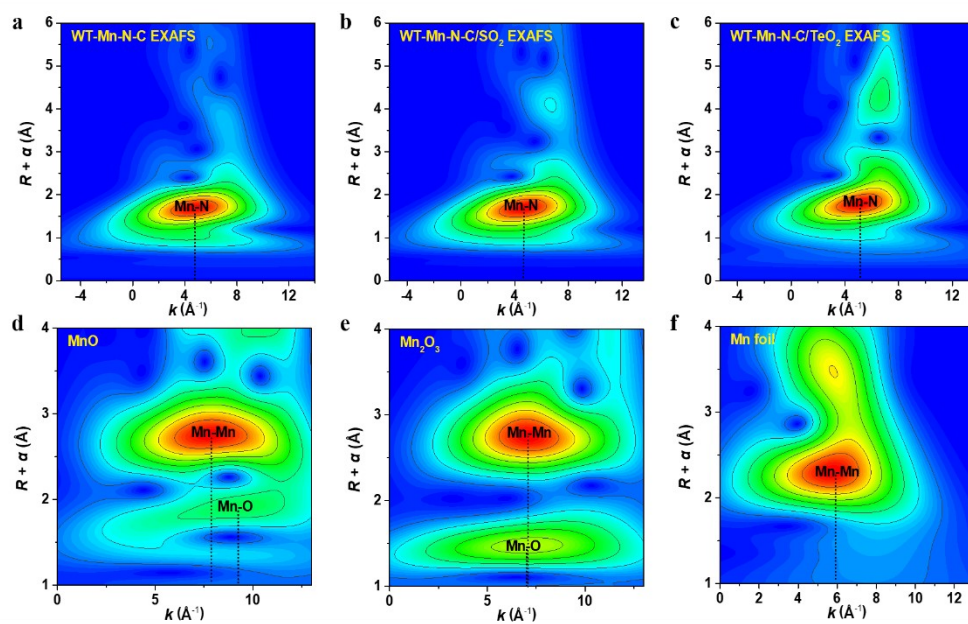


Figure S11. WT-EXAFS signals of (a) Mn-N-C, (b) Mn-N-C/SO₂, (c) Mn-N-C/TeO₂, (d) MnO, (e) Mn₂O₃ and (f) Mn foil.

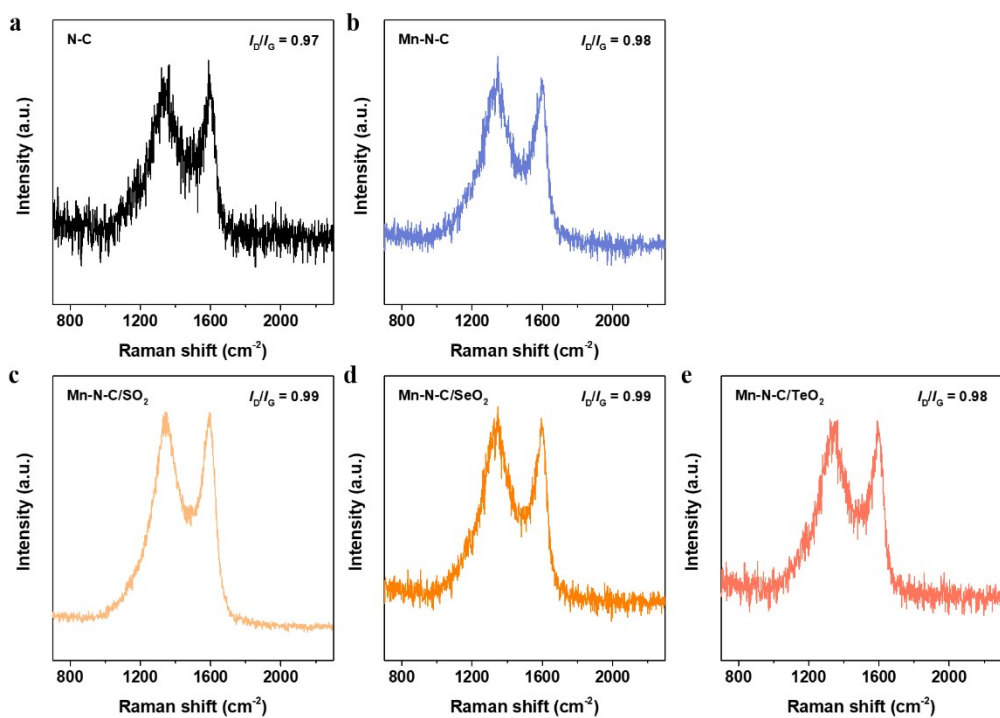


Figure S12. Raman spectra of (a) N-C, (b) Mn-N-C, (c) Mn-N-C/SO₂, (d) Mn-N-C/SeO₂ and (e) Mn-N-C/TeO₂. The intensity ratios between D band to G band (~1) indicate that the incorporation of XO₂ groups does not alter the carbon plane size of Mn-N-C catalysts.

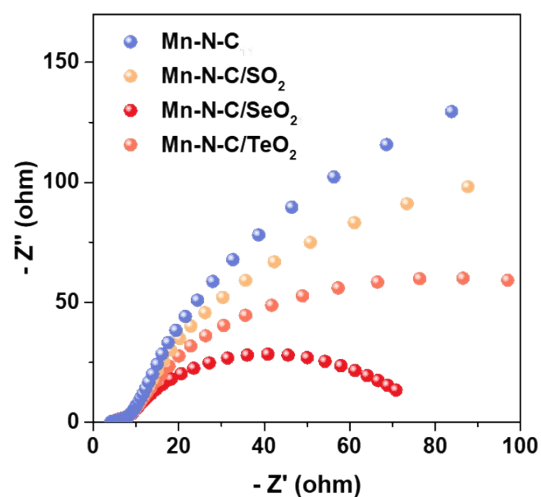


Figure S13. EIS spectra of Mn-N-C and Mn-N-C/ XO_2 at $0.8 V_{RHE}$ collected from 100 kHz to 0.1 Hz. The electrical conductivity of Mn-N-C/ XO_2 is lower than that of Mn-N-C, indicating that Mn-N-C/ XO_2 exhibits more efficient electron transfer and faster ORR kinetics after the incorporation of XO_2 . Among them, Mn-N-C/SeO₂ has the lowest electrical conductivity, demonstrating the highest electron transfer efficiency and the fastest ORR kinetics.

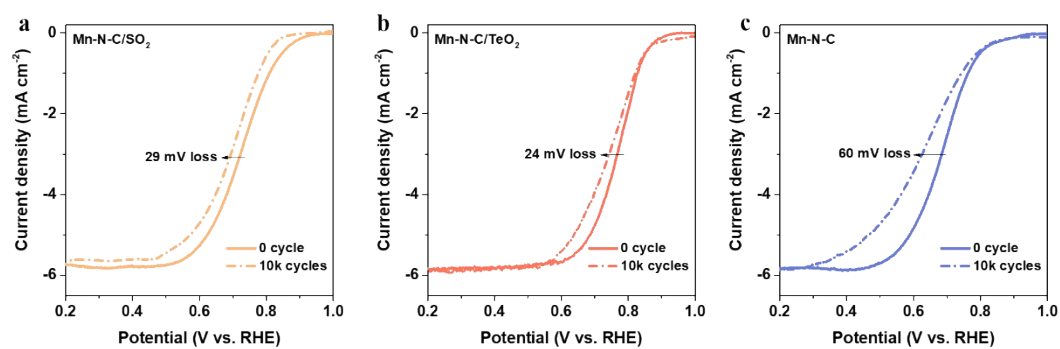


Figure S14. LSV curves of (a) Mn-N-C, (b) Mn-N-C/SO₂ and (c) Mn-N-C/TeO₂ catalyst at the initial cycle and after 10,000 cycles.

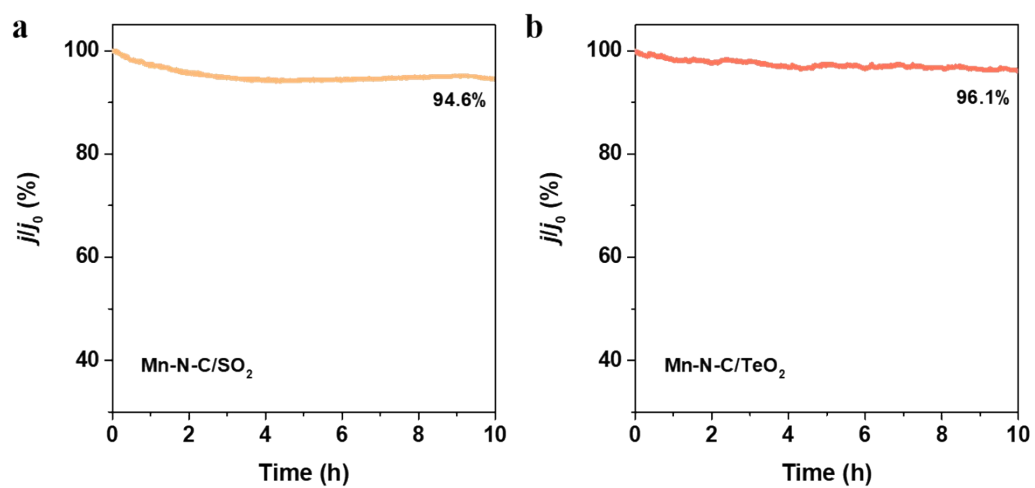


Figure S15. Electrocatalytic stability testing of (a) Mn-N-C/SO₂ and (b) Mn-N-C/TeO₂ by chronoamperometry from 0.6 V_{RHE} to 1.0 V_{RHE}.

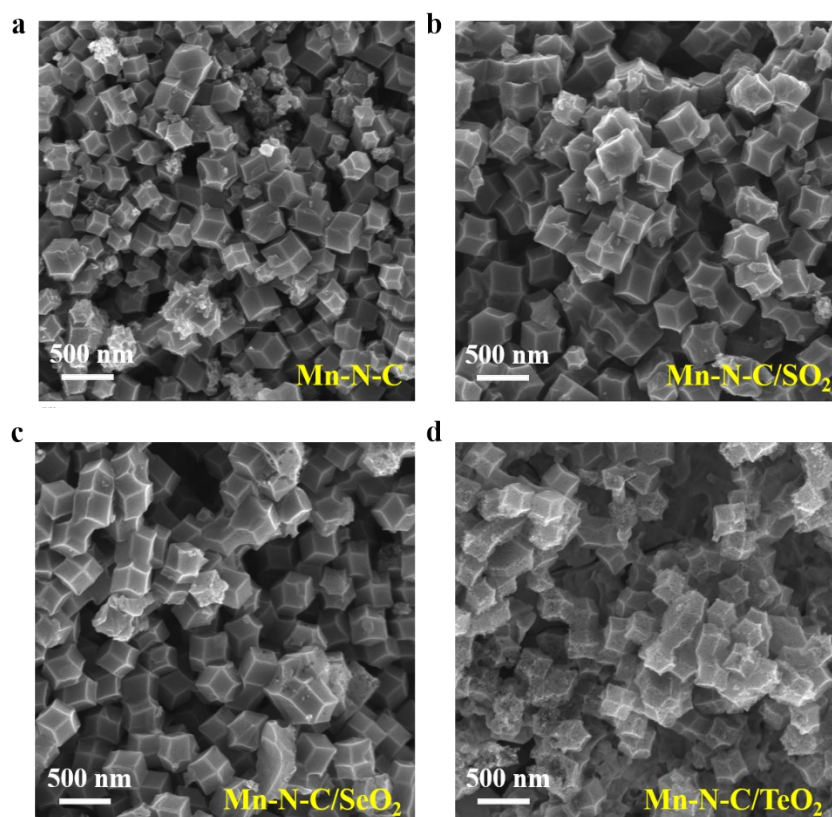


Figure S16. SEM image of (a) Mn-N-C, (b) Mn-N-C/SO₂, (c) Mn-N-C/SeO₂ and (d) Mn-N-C/TeO₂ catalysts under long-term post-ORR conditions. After long-term stability testing for the ORR, both Mn-N-C and Mn-N-C/XO₂ catalysts maintained the MOF octahedral structure. This indicates that the carbon matrix formed by high-temperature calcination of the MOF has acid resistance. Furthermore, during the acidic ORR reaction and stability tests, the catalysts retained their original morphology, suggesting that the enhanced stability of the catalyst is not due to the stability of the carbon matrix.

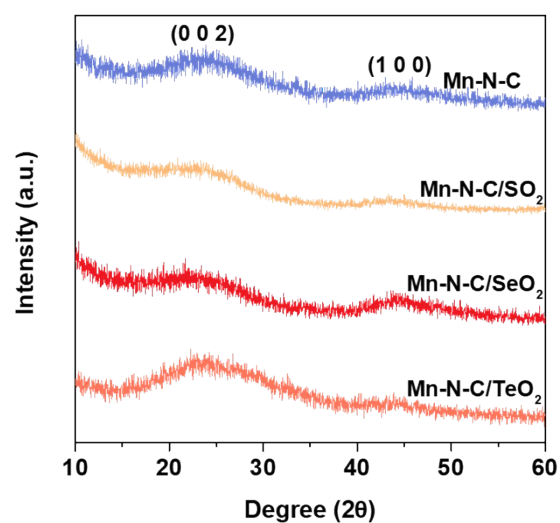


Figure S17. XRD patterns of (a) N-C, Mn-N-C, Mn-N-C/SeO₂ catalysts and (b) Mn-N-C/SO₂, Mn-N-C/TeO₂ catalysts under long-term post-ORR conditions. After long-term stability testing for the ORR, the XRD patterns of both Mn-N-C and Mn-N-C/XO₂ catalysts do not exhibit distinct crystalline peaks, maintaining the characteristic (0 0 2) and (1 0 0) peaks of the carbon matrix. This indicates that after the long-term stability test, the Mn in both Mn-N-C and Mn-N-C/XO₂ catalysts remains in a single-atom form without aggregation. after long-term stability testing for the ORR.

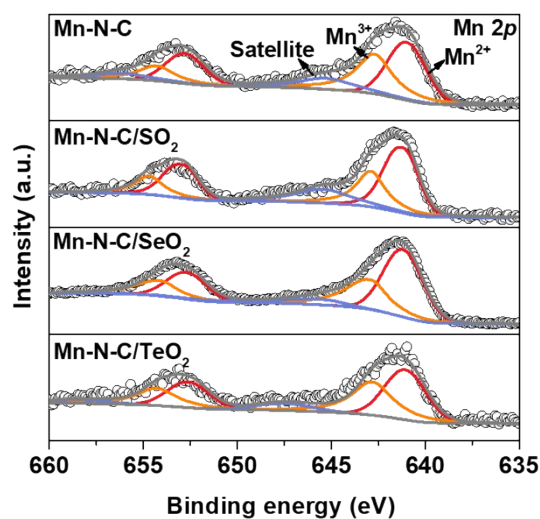


Figure S18. High-resolution (a) Mn $2p$ spectra of Mn-N-C and Mn-N-C/ XO_2 catalysts under long-term post-ORR conditions. After long-term post-ORR, the content of Mn^{3+} in the Mn-N-C catalyst increased to a level higher than that of Mn^{2+} , while the Mn-N-C/ XO_2 catalysts remained predominantly in the +2 oxidation state. Among them, the Mn-N-C/ SeO_2 catalyst exhibited the highest content of Mn^{2+} , indicating that after long-term ORR stability testing, the Mn-N-C/ SeO_2 catalyst was able to maintain Mn in a lower oxidation state.

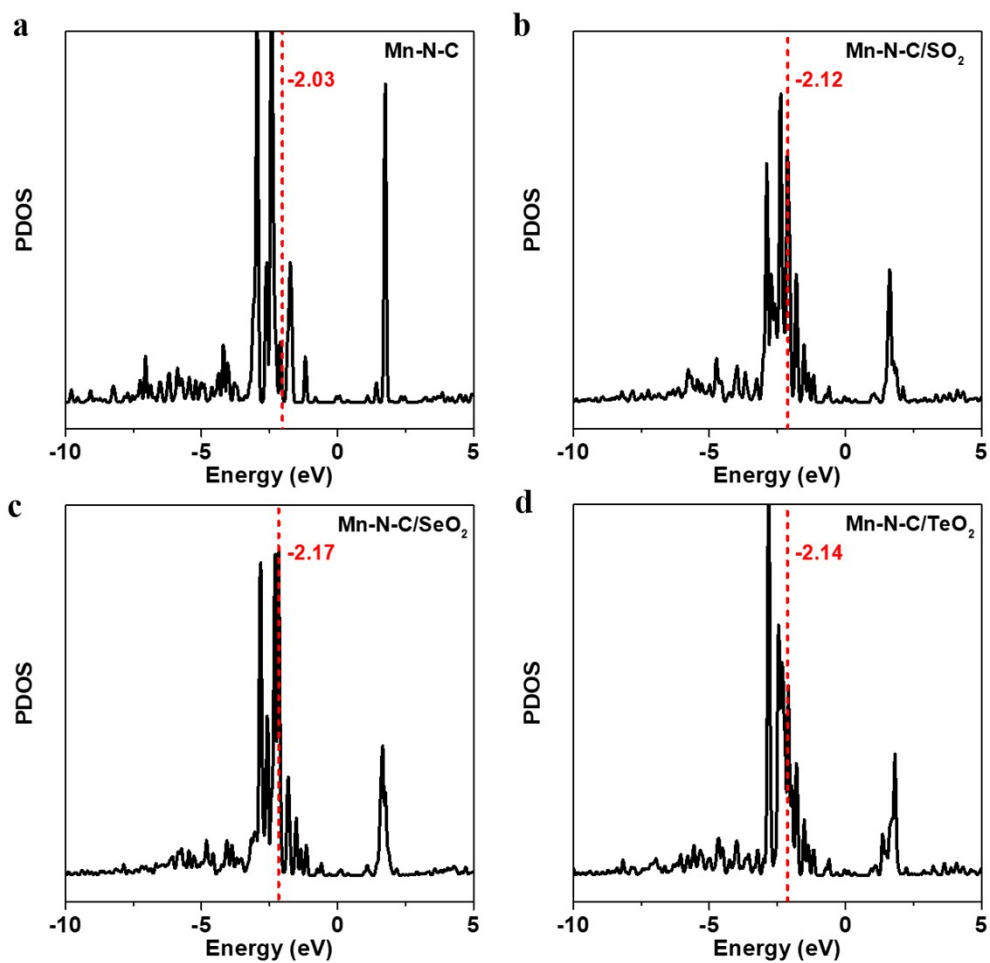


Figure S19. Projected density of states on Mn *d*-orbitals in (a) Mn-N-C, (b) Mn-N-C/SO₂, Mn-N-C/SeO₂ and (d) Mn-N-C/TeO₂ catalyst.

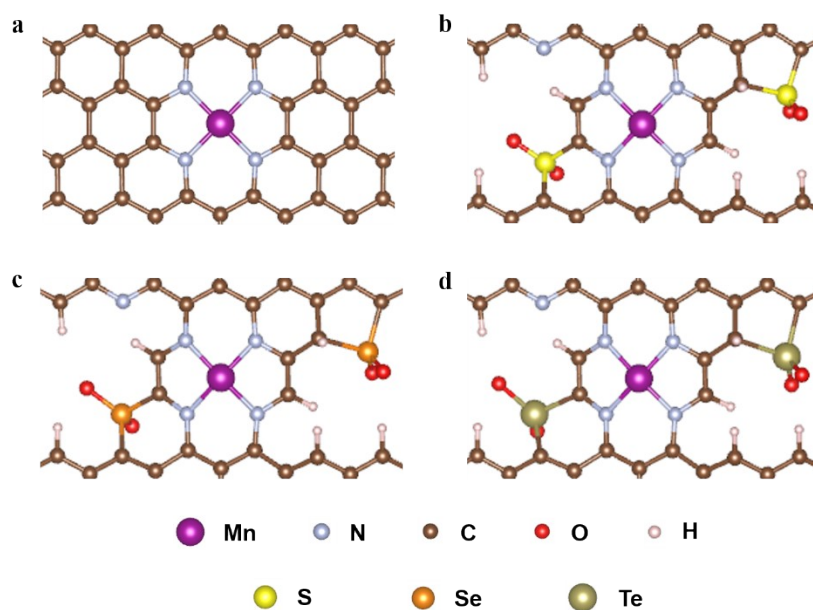


Figure S20. The calculated atomic structures of the Mn-N-C and Mn-N-C/XO₂ catalyst models after the relaxation. (a) Mn-N-C, (b) Mn-N-C/SO₂, (c) Mn-N-C/SeO₂ and (d) Mn-N-C/TeO₂.

Supplementary Tables

Table S1. XPS peak fitting results of Mn-N-C and Mn-N-C/XO₂ catalysts.

Sample	Peak area (eV)		Ratio (Mn ²⁺ /Mn ³⁺)
	Mn ²⁺	Mn ³⁺	
Mn-N-C	2989.07	2052.64	1.11
Mn-N-C/SO ₂	2406.4	1170.06	2.05
Mn-N-C/SeO ₂	2507.07	1058.12	2.37
Mn-N-C/TeO ₂	2803.63	1311.64	2.14

Table S2. Analysis of the contents of XO₂ in Mn-N-C catalysts by XPS.

Catalyst	C (at%)	N (at%)	O (at%)	X (at%)	Mn (at%)
Mn-N-C	84.55	10.82	3.70	--	0.93
Mn-N-C/SO ₂	81.64	10.74	4.91	1.80	0.91
Mn-N-C/SeO ₂	81.70	10.85	4.78	1.84	0.92
Mn-N-C/TeO ₂	81.82	10.99	4.48	1.83	0.88

Note that X stands for S, Se and Te element in Mn-N-C/SO₂, Mn-N-C/SeO₂ and Mn-N-C/TeO₂, respectively.

Table S3. Summary of Mn contents in Mn-N-C and Mn-N-C/XO₂.

Catalyst	Mn (wt%)
Mn-N-C	3.05
Mn-N-C/SO ₂	3.06

Mn-N-C/SeO ₂	3.09
-------------------------	------

Mn-N-C/TeO ₂	2.96
-------------------------	------

Table S4. Fitting parameters of EXAFS of Mn-N-C and Mn-N-C/XO₂ catalysts.

Catalyst	Scattering paths	CN	R (Å)	E_0 (eV) (S_0^2)	σ^2 (Å ²)	R -factor
Mn-N-C	Mn-N	4.2	2.02	1.36 (1)	0.005	0.020
Mn-N-C/SO ₂	Mn-N	4.2	2.15	-3.70 (1)	0.020	0.019
Mn-N-C/SeO ₂	Mn-N	4.0	2.23	1.78 (1)	0.030	0.007
Mn-N-C/TeO ₂	Mn-N	3.8	2.16	4.20 (1)	0.002	0.020

Note: CN, coordination number; R , distance to the neighboring atom; σ^2 , mean square relative displacement; E_0 , inner potential correction; R -factor indicates the goodness of the fit. According to the experimental EXAFS fit of Mn foil by fixing CN as the known crystallographic value. This value was fixed during EXAFS fitting, based on the known structure of Mn. Fitting range: $3.2 \leq k$ (Å⁻¹) ≤ 10.0 and $1 \leq R$ (Å) ≤ 2.5 . A reasonable range of EXAFS fitting parameters: $0.700 < S_0^2 < 1.000$; $CN > 0$; $\sigma^2 > 0$ Å²; $|\Delta E_0| < 15$ eV; R -factor ≤ 0.02 .

Table S5. Comparison of ORR and PEMFC performance between the Mn-N-C/SeO₂ and recently reported catalysts.

Catalyst	Active sites	RDE performance			Ref.
		E _{1/2}	Electrolyte	Stable test	
Mn-N-C/SeO₂	MnN₄	0.79 V	0.5M H₂SO₄	11 mV (10k cycles)	This work
Mn-SAs/NC ^a	Mn	0.76 V	0.5M H ₂ SO ₄	10 mV (5k cycles)	1
MnCo-N-C ^b	MnCo	0.75 V	0.5M H ₂ SO ₄	25 mV (5k cycles)	2
FeMn _{ac} /Mn-N ₄ C ^c	Mn	0.78 V	0.5M H ₂ SO ₄	84% (60k second)	3
MnNCS-4-800 ^d	MnN	0.75 V	0.5M H ₂ SO ₄	20 mV (10k cycles)	4
MnNC	MnN	0.8 V	0.5M H ₂ SO ₄	17 mV (30k cycles)	5

Note: ^a Mn single atom anchored on N-doped porous carbon. ^b a Mn, Co and N co-doped carbon catalyst. ^c Mn-based single atom catalyst with atomically dispersed Mn-N₄ sites and FeMn atomic clusters. ^d Mn sites on carbon nanosheet, 4 represents the molar ratio of MnCl₂/ hexamine, 800 represents the pyrolysis temperature.

Table S6. The Mn-N bond lengths of the calculated Mn-N-C and Mn-N-C/XO₂ catalyst models after the relaxation.

Catalyst	Bond length (Å)			
	d ₁	d ₂	d ₃	d ₄
Mn-N-C	1.91	1.91	1.91	1.91
Mn-N-C/SO ₂	1.93	1.93	1.94	1.92
Mn-N-C/SeO ₂	1.97	1.93	1.95	1.92
Mn-N-C/TeO ₂	1.94	1.93	1.95	1.92

Note: d₁, d₂, d₃ and d₄ represent the Mn-N bond lengths in the atomic model of Figure S16, corresponding to the top left, top right, bottom left, and bottom right, respectively.

Table S7. XPS peak fitting results of Mn-N-C and Mn-N-C/XO₂ catalysts after long-term post-ORR conditions.

Sample	Peak area (eV)		Ratio (Mn ²⁺ /Mn ³⁺)	Pristine ratio
	Mn ²⁺	Mn ³⁺		
Mn-N-C	2627.56	2986.12	0.88	1.11
Mn-N-C/SO ₂	11103.97	8424.72	1.26	2.05
Mn-N-C/SeO ₂	23006.54	13349.15	1.72	2.37
Mn-N-C/TeO ₂	1637.47	1090.25	1.49	2.14

1. Huo J, *et al.* Atomically dispersed Mn atoms coordinated with N and O within an N-doped porous carbon framework for boosted oxygen reduction catalysis. *Nanoscale* **15**, 5448-5457 (2023).
2. Chao G, *et al.* Nitrogen-coordinated single-atom catalysts with manganese and cobalt sites for acidic oxygen reduction. *Journal of Materials Chemistry A* **10**, 5930-5936 (2022).
3. Liu H, *et al.* Decorating Single-Atomic Mn Sites with FeMn Clusters to Boost Oxygen Reduction Reaction. *Angew Chem Int Ed Engl* **62**, e202214988 (2023).
4. Zhong G, *et al.* Atomically dispersed Mn–Nx catalysts derived from Mn-hexamine coordination frameworks for oxygen reduction reaction. *Carbon Energy*, (2024).
5. Li C-J, Shan G-C, Guo C-X, Ma R-G. Design strategies of Pd-based electrocatalysts for efficient oxygen reduction. *Rare Metals* **42**, 1778-1799 (2023).